THE JOURNAL OF PHYSICAL CHEMISTRY C

pubs.acs.org/JPCC Article

Silicate Bond Characteristics in Calcium−Silicate−Hydrates Determined by High Pressure Raman Spectroscopy

David W. Gardner, Jiaqi Li, Ali Morshedifard, Saeed Masoumi, Mohammad Javad Abdolhosseini Qomi, Paulo J. M. Monteiro, Roya Maboudian, and Carlo Carraro*

Cite This: J. Phys. Chem. C 2020, 124, 18335−18345 Read Online

ACCESS | Metrics & More | Article Recommendations | Supporting Information

ABSTRACT: The mechanical and thermal properties of the gigatonnes of concrete produced annually are strongly affected by the anharmonicity of the chemical bonds in its main binding phase, nanocrystalline calcium−(alumino−)silicate−hydrate (C−(A−)S−H). Improvements in C−(A−)S−H design increasingly depend on simulations utilizing a set of effective interatomic forces known as "CSH-FF", yet these assumptions have never been directly examined at the chemical bond level, and there is no guidance for their improvement. In this work, we use high-pressure Raman spectroscopy to directly measure bond anharmonicity in a representative series of C−(A−)S−H samples with varying composition and two natural model minerals, 14 Å tobermorite and xonotlite. We find that structural water molecules effectively scatter thermal energy, providing a heuristic for improving the thermal resistance of concrete. A comparison of experimental and calculated bond anharmonicities shows that a stiffer Si−O interaction would improve the transferability of CSH-FF to the thermal properties of C−(A−)S−H. High-pressure Raman spectroscopy is suggested to improve the calculations of C−S−H and to characterize other complex, nanocrystalline materials.

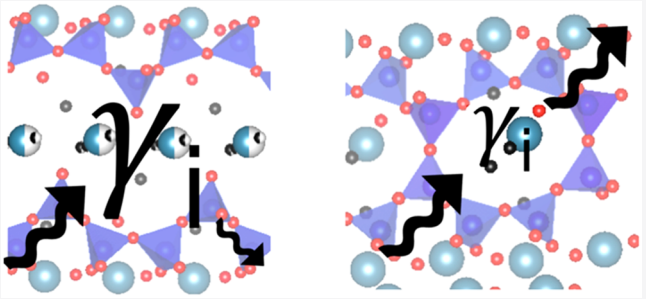

INTRODUCTION

Concrete production is responsible for nearly 10% of anthropogenic carbon dioxide worldwide,[1−3] because of the direct manufacture of Portland cement (the principal binder in concrete) and because of the processes affiliated with its deployment. The primary binding phase in Portland cement is calcium−(alumino−)silicate−hydrate (C−(A−)S−H),[4,5] which controls the mechanical and thermal properties (e.g., thermal conductivity and thermal expansivity) of the resulting, hardened concrete.

Throughout this manuscript we will use cement notation for our samples. Cement notation describes the reagents used to prepare the cement and/or the composition of the cement precipitates, where C = CaO, S = SiO_2, A = Al_2O_3, and H = hydrate or H_2O.

Modifying the structure of the binding phase C−(A−)S−H can affect the bulk modulus by at least a factor of 2,[6] and its thermal conductivity can have as large an effect as added aggregates on the final thermal conductivity of hardened concrete.[7,8] Unfortunately, the thermal resistance and compressive strength of classic C−(A−)S−H have a negative correlation (because these properties have opposite correlations with density), so new insights are needed to develop a binding phase that can provide sufficient thermal insulation and mechanical strength to address the growing heating and air conditioning energy consumption of buildings.[4,9,10]

C−(A−)S−H is a nanocrystalline material whose atomic structure and mechanical properties are acceptably modeled with a so-called defective tobermorite structure.[5] The 14 Å tobermorite has a layered structure (Figure 1a) comprising two-dimensional calcium oxide sheets sandwiched between one-dimensional dreierketten chains of silica tetrahedra. The tetrahedra can be in a paired environment directly on the calcium oxide sheet or in a bridging environment offset from the paired tetrahedra along the *c*-axis. Because each silica tetrahedron is bound to two other silica tetrahedra they are all "Q^2" according to standard notation.[11] If there is aluminum in the structure, the aluminum substitutes for a bridging Q^2 silica tetrahedron without affecting the rest of the structure, except for a slight increase in *b* axis because of slightly longer bond lengths.[6,12,13] Between these silica chains is a layer of strongly adsorbed water and charge-balancing interlayer calcium ions.[14] Although the chains are infinitely long in 14 Å tobermorite, there are defects in C−S−H in the form of missing bridging tetrahedra, leading to "Q^1" tetrahedra at the end of the chains

Received: May 21, 2020
Revised: July 22, 2020
Published: July 24, 2020

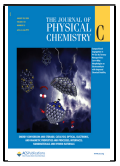

https://dx.doi.org/10.1021/acs.jpcc.0c04563
J. Phys. Chem. C 2020, 124, 18335−18345

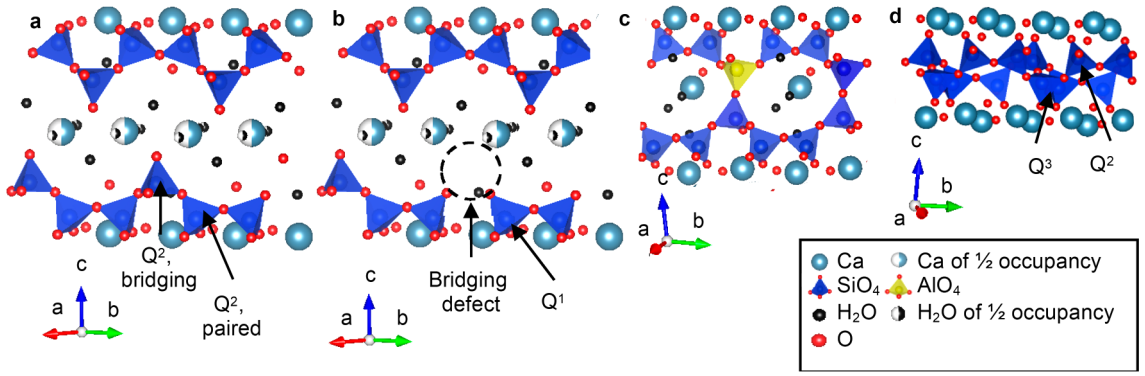

Figure 1. (a) Crystal structure of 14 Å tobermorite,[15,16] (b) proposed structure of C−S−H based on 14 Å tobermorite, (c) proposed structure of cross-linked C−(A−)S−H, (d) crystal structure of xonotlite.[17] Specific Si tetrahedra are labeled using standard notation.

(Figure 1b). Aluminum can induce cross-linking of adjacent Si chains, leading to a cross-linked structure (Figure 1c).[6]

If the interlayer of 14 Å tobermorite is completely collapsed, water molecules and interlayer calcium ions are removed, and the opposing silica chains cross-link, the resulting structure is xonotlite (Figure 1d). There are two environments for silica tetrahedra in xonotlite: those in the Q^2 environment, which resemble the paired tetrahedra of 14 Å tobermorite, and those in the Q^3 environment, bound to a silica tetrahedron on both sides approximately along the *b*-axis and one silica tetrahedron along the *a*-axis. It should be noted that there are very similar structural motifs between the samples, including the dreierketten silica chains and calcium oxide sheets.

Despite their limitations, simulations have provided valuable insight in the physics of cementitious materials at small scales. These simulations prescribe all interatomic interactions through force fields such as CSH-FF,[18] ClayFF,[19] or ReaxFF.[20] An in-depth review of these force fields is provided in Mishra et al.[21] The most widely used force field, CSH-FF, is a reparameterization of ClayFF to improve second order properties (e.g., elastic constants) based on *ab initio* calculations of 11 Å tobermorite. In this force field, atoms interact via electrostatic and van der Waals potentials, and covalent harmonic interactions exist only for water and hydroxyl molecules. This force field was trained solely based on first-principles calculations and its predictive capability was checked against elastic, strength, and creep properties measured in nanoindentation and high-pressure X-ray diffraction experiments.[6,10,22,23] Presently, we rely on spectroscopic experiments[24,25] of highly crystalline materials and brute-force empirical methods, for example, ab initio calculations of crystalline minerals, for force field refinement, but there is little guidance for the structural−chemical regimes of validity of the force fields in C−(A−)S−H and whether linear extrapolations can be safely performed.

Raman spectroscopy is a direct probe of lattice vibrations. Lattice vibrational frequencies describe the local bonding environment through the position of their energy bands.[26] This technique is commonly employed to study crystal structure,[27] orientation,[28] and chemical composition.[11,29,30] High-pressure Raman spectroscopy, when coupled with high-pressure X-ray diffraction (HP XRD), can describe the anharmonicity of interatomic interactions in a given sample as described below, which has implications for parameters of immediate practical interest, such as bond character and thermal conductivity.

Consider an anharmonic oscillator described by a two-body potential, $U(l)$, where the bodies are separated by a distance l with effective attractive and repulsive terms[31] given in eq 1:

$$U(l) = U_0 - al^{-A} + rl^{-R} \tag{1}$$

where U_0 is a reference energy, a is the coefficient for the attractive term, A is the power dependence of the attractive potential, r is the coefficient for the repulsive term, and R is the power dependence of the repulsive term. The frequency of a given vibration, ω_i, changes with pressure, P, as does the associated volume; the ratio of the relative change in frequency to the relative change in the associated volume is called the mode Grüneisen parameter, γ_i. When strain is small, the mode Grüneisen parameter of the particular oscillator is related to the exponents in eq 1 as follows:[31]

$$\gamma_i = -\frac{V_i}{\omega_i}\frac{d\omega_i}{dV_i} = -\frac{V_i}{\omega_i}\frac{d\omega_i/dP}{dV_i/dP} = \frac{A+R+3}{6} \tag{2}$$

where V_i is the volume that is changing during the vibration, *not* the volume of the unit cell.[32] Higher values of γ_i indicate softer, more anharmonic interactions. The mode Grüneisen parameter is 3.5 for 6−12 Lennard-Jones interactions, ∼2.2 for ionic interactions, and ∼1 for covalent interactions.[31] The pressure derivatives make explicit how we can combine separately obtained data for vibrational frequency (by high-pressure Raman spectroscopy) and for volume (by high-pressure XRD) to determine the Grüneisen parameter.

The bulk Grüneisen parameter is related to the mode Grüneisen parameter of individual oscillators of eq 2 through eqs 3a−3c:

$$\gamma = \frac{\sum_i N_i c_{Vi}\gamma_i}{\sum_i N_i c_{Vi}} = \frac{\alpha B_0}{\rho C_V} \tag{3a}$$

$$\frac{c_{Vi}}{k_B} = X_i^2\frac{\exp(X_i)}{(\exp(X_i)-1)^2} \tag{3b}$$

$$X_i = \frac{\hbar\omega_i}{k_B T} \tag{3c}$$

where c_{Vi} is the constant-volume heat capacity of a given oscillator, N_i is the number of such oscillators, α is the constant-pressure thermal expansivity, B_0 is the bulk modulus, ρ is the density, C_V is the bulk constant-volume heat capacity, k_B is the Boltzmann constant, X_i is the ratio of vibrational to thermal energies, and $\hbar$ is the reduced Planck's constant. Note

https://dx.doi.org/10.1021/acs.jpcc.0c04563
J. Phys. Chem. C 2020, 124, 18335−18345

that eq 3a is for the full unit cell of a pure material and eq 2 is for an individual oscillator.

The mode Grüneisen parameter is also closely linked to thermal conductivity of a material. The thermal conductivity of a material is given by the Boltzmann transport equation in eq 4a,[33] and the relation to the Grüneisen parameter is given by eq 4b[34,35] when phonon−phonon scattering processes dominate:[4]

$$\kappa_{\mathrm{BTE}} = \sum_i c_{Vi} v_i^2 \tau_i \tag{4a}$$

$$\tau_i = \frac{M v_i^2}{\gamma_i^2 k_B T} \Omega \tag{4b}$$

where κ_{BTE} is the thermal conductivity, v_i is the group velocity of the phonon, τ_i is the relaxation time of the phonon, M is the reduced mass, and Ω is a factor that accounts for thermal occupation.[34,35] The inverse-square dependence in eq 4b between the relaxation time and the mode Grüneisen parameter is also valid for scattering at grain boundaries and at stacking faults,[35] but with different prefactors.

Roughly 30% of thermal energy transport in C−(A−)S−H occurs through the scattering mechanisms[4,7] of long-wavelength phonons below 100 cm^{-1} (the so-called boson peak) and the rest is controlled by diffusive modes between 100 and 600 cm^{-1}. Phonon interactions occur through the nonlinear (cubic and higher order) terms in the interatomic potentials, and manifest themselves macroscopically in measurable properties such as thermal conductivity and volume expansivity. Direct experimental access to interatomic bond anharmonicities is thus of considerable importance in the development and refinement of force fields capable of predicting important material properties. While we cannot directly access the low-energy vibrational modes responsible for heat transfer in our present experimental setup, we can measure the effects of anharmonicities on higher frequency modes through the measurement of their Grüneisen parameters. The approach is supported by several surveys of other oxides showing that the mode Grüneisen parameter of low wavenumber modes correlates with the mode Grüneisen parameters of high wavenumber modes.[36−39]

In this work, we present the high pressure Raman spectra of nanocrystalline C−(A−)S−H of which the calcium-to-silicon ratios (Ca/Si) range from 0.8 to 1.3, Al/Si ratios range from 0 to 0.1, and synthesis temperatures range from 20 to 80 °C, as well as that of two natural minerals: 14 Å tobermorite (Figure 1a), a calcium silicate hydrate mineral with formula $Ca_5Si_6O_{16}(OH)_2{\cdot}7H_2O$ often used as a model for C−S−H; and xonotlite (Figure 1d), a calcium silicate hydrate mineral with formula $Ca_6Si_6O_{17}(OH)_2$ that is present in concretes cast at high temperature and oil well cement slurry[40,41] and represents an extreme case for calcium silicate hydrate minerals in terms of low basal spacing, high degree of silica tetrahedra polymerization, and low water content. These samples are summarized in Table 1. In particular, we track the vibrations of silica tetrahedra, because these display the greatest tunability within the structure and are the stiffest elements in C−(A−)S−H.[23] We compare the experimental results with calculated shifts in frequency with pressure using CSH-FF for a set of structures similar to the C−S−H samples and three crystalline samples, 14 Å tobermorite, 11 Å tobermorite, and xonotlite. These high-pressure Raman spectra are used to learn directly about anharmonic effects and indirectly about thermal transport in calcium silicates. We also show how the high-pressure Raman spectra can be used to improve calculations of these materials' mechanical and thermal properties.

Table 1. Description of Samples Studied in This Work

Sample Name	Ca/(Si+Al)	Al/Si	Synthesis Temperature	Cross-Linked?
natural xonotlite	1.0		N/A	√
natural 14 Å tobermorite	0.83		N/A	
80 °C C−S−H	1.0		80 °C	
0.05 Al/Si C−A−S−H	1.0	0.05	80 °C	√
0.1 Al/Si C−A−S−H	1.0	0.10	80 °C	√
0.8 Ca/Si C−S−H	0.8		20 °C	
1.0 Ca/Si C−S−H	1.0		20 °C	
1.3 Ca/Si C−S−H	1.3		20 °C	

METHODS

Sample Preparation. The 14 Å tobermorite specimen was a natural specimen obtained from Crestmore, California. The preparation and characterization for the C−(A−)S−H specimens in this work can be found elsewhere.[6,23,42,43] The sample 80 °C C−S−H, which is reported to be a mixture of two crystals with interlayers 12.2 and 13.8 Å with a 5:1 relative abundance, respectively, was treated to be homogeneous in the 12.2. Å basal spacing. The xonotlite specimen was a natural specimen obtained from Christmas, Arizona. Note that while the 1.3 Ca/Si C−S−H was designed *in silico* starting from 9 Å tobermorite,[23] we chose xonotlite as the "extreme case" of low basal spacing and silica polymerization because it has a distinct but similar structure to the C−S−H samples, whereas 9 Å tobermorite has a similar structure to 1.3 Ca/Si C−S−H and the effect of crystallinity can be understood by comparing 14 Å tobermorite and 0.8 Ca/Si C−S−H. All samples were stored in vacuum when not in use. The C−S−H specimens were characterized by nuclear magnetic resonance NMR[13] and high-pressure XRD;[23] the 14 Å tobermorite sample was characterized by high-pressure XRD,[44] and the xonotlite sample was characterized by high-pressure XRD to support this work. A summary of the samples' mechanical properties is given in Table S1.

Ambient Raman Spectra. Ambient Raman spectra were recorded by loading the powders onto glass slides with care to ensure that the glass slides did not contribute to the recorded Raman spectra. The spectra were acquired in backscattering geometry at room temperature with a JY-Horiba Labram spectrometer with an 1800 groove/mm grating. A HeNe laser (632.8 nm) provided the excitation line through an Olympus BX41 confocal microscope, which was focused on the sample by a 50× long working distance objective. The spot size was less than 1 μm. For the orientation-dependent 14 Å tobermorite spectra, a dilute suspension of 14 Å tobermorite crystals in ethanol was prepared and dropcast onto a gold substrate. Ethanol was chosen because the mineral is stable in it and because ethanol evaporates quickly. Once a single 14 Å tobermorite crystal was located, the sample was carefully rotated so that the longest dimension of the 14 Å tobermorite crystal—the nominal principal axis—was parallel (i.e., 0°) to the polarization of the light.[28] Five scans were recorded on the range 0°−90° with the angle corresponding to the angle made by the longest dimension of the 14 Å tobermorite needle (likely corresponds to its *c*-axis[45]) with respect to the

https://dx.doi.org/10.1021/acs.jpcc.0c04563
J. Phys. Chem. C 2020, 124, 18335−18345

polarization of the light. The measurements were repeated qualitatively for three 14 Å tobermorite crystals.

High-Pressure Raman Spectra. The specimens were loaded into a BX90 diamond anvil cell by a standard procedure with a pressure medium, either a 4:1 volume/volume mixture of methanol to ethanol, or silicone oil.[23] It was necessary to use multiple pressure media so that the mineral peaks could be observed without interference from the pressure media peaks. The standard ruby lines R1 and R2 could not be used for pressure measurement when measuring the minerals in this study because the high laser power used for the calcium silicate hydrate samples activated the ruby fluorescence, which had an unacceptable level of convolution with the samples' weak Raman lines. Instead, the pressure in the diamond anvil cell was obtained from the Raman frequency of the top diamond culet (Figure S1). Focus on the top diamond was obtained by first focusing on the face of the diamond open to air, then panning down until the first feature of the gasket was in focus, then panning up ~0.01 mm. The pressure based on the top diamond was calibrated by measuring the Raman frequency of the diamond with the known pressure gauge of the ruby R1 and R2 fluorescence peaks. The obtained calibration curve aligns with those obtained by other groups.[46] Calibrating the diamond is preferable to using a literature curve because the shift with pressure can vary between diamond samples.[46]

High-pressure Raman spectra were acquired in back-scattering geometry at room temperature with the same JY-Horiba Labram spectrometer described above. Three scans were obtained per sample: the first recorded the frequency window around the diamond line while focused on the top diamond culet, the second recorded the frequency window around the silicate regions while focused on the specimen, and the third was a repeat of the first frequency window while focusing on the top diamond culet to verify that the pressure had not changed.

Peaks were integrated with a straight-line baseline and with the use of a 50/50 mixed Gaussian−Lorentzian function. When calculating the least-squares regression line to determine $d\omega/dP$ [=] cm^{-1}/GPa throughout, only points from pressures less than 3 GPa were considered so that the error associated with the pressure measurement and the decreased signal intensity at higher pressure did not meaningfully impact the results.

High-Pressure XRD. High-pressure XRD studies of 14 Å tobermorite and C−(A−)S−H have been presented previously.[6,23,44] High-pressure XRD of xonotlite was recorded at beamline 12.2.2 at the Advanced Light Source (ALS) at Lawrence Berkeley National Laboratory. The specimen was loaded into a BX90 diamond anvil cell by a standard procedure with 4:1 volume/volume methanol to ethanol pressure medium. Hydrostatic pressure was determined by the ruby fluorescence method.[23] XRD phase analysis can be found in previous characterization of the specimens.[23] The standard error of the fit axis compressibilities is typically less than five percent of the axis compressibility.

Thermogravimetric Analysis. Thermogravimetric analysis (TGA) of the samples was reported previously for the room-temperature synthesized[47] and 80 °C synthesized samples[13] to determine the number of water molecules per silicon atom for samples equilibrated at 30 °C. We fit the existing differential TGA plots in the region 50 °C−250 °C to two Gaussians. The curve centered near or less than 100 °C was assigned to extragranular or gel water, and the curve centered above 100 °C was assigned to interlayer water molecules. However, the binding energy of the interlayer water molecules may change as more and more are evaporated, so we take the mass perecent of the interlayer water to be the difference between total mass loss at 500 °C and the numerical mass loss of the gel water. Once the mass percent of interlayer water is determined, a mass balance with the remaining mass determines the number of interlayer water molecules. The values are reported in Table S2, and an example differential TGA plot and the fit Gaussians are given in Figure S2. The calculated values agree well with intuition; nearly all points lie within the line bounded by 14 Å tobermorite, normal 11 Å tobermorite, 9 Å tobermorite, and xonotlite.

Atomistic Simulations. The widely used transferrable CSH-FF potential was used to describe interatomic interactions[4,18,21,48−51] for all simulations reported here. This force field was previously used to study elastic,[10,23,52] fracture,[53] and thermal properties[4] as well as the molecular origins of cohesion[54−56] in C−S−H. Structures of xonotlite polytype A-1[17] and tobermorite 14 Å[15] are readily prepared. The three C−S−H samples were modeled as explained in ref 23. Molecular dynamics (MD) simulations in the NPT ensemble were run in LAMMPS[57] to obtain adequate statistics for calculating cell parameters as a function of pressure. Vibrational frequencies and modes were calculated using the exact second derivatives of the system's potential energy as implanted in GULP.[58,59] Similar to previous work,[22] enthalpy optimizations were carried out prior to both MD and frequency calculations. Simulations were carried out at different integer values of pressure from 0 to 5 GPa for mechanical properties and frequency calculations. For MD runs, a Nose-Hoover thermostat and barostat with a time step of 1 fs were used. Further simulation details can be found in the Supporting Information.

RESULTS AND DISCUSSION

Peak Assignments in Raman Spectra. Table 2 provides the peak assignments at ambient pressure for the relevant spectral regions studied in this work. CaO and SiO deformations were not intense enough to be measured reliably at high pressure and are not discussed. The findings are in good agreement with previous characterization of similar samples for xonotlite,[60] tobermorite,[61] and C−(A−)S−H.[11,29,30,61]

Table 2. Peak Wavenumbers and Assignments at Ambient Pressure

Raman Shift (cm^{-1})	Assignment[11,29,30,61]
593	xonotlite Q^3 Si−O−Si bending
667−695	Q^2 Si−O−Si bending
800−900	Q^1 Si−O symmetric stretch
990−1040	Q^2 Si−O symmetric stretch
1077	calcium carbonate
3611	xonotlite OH stretch

Figure 2 provides representative ambient Raman spectra of the studied samples.

We observe three distinct peaks in the 14 Å tobermorite spectrum at 998, 1033, and 1058 cm^{-1} (Figure S3), in contrast to Kirkpatrick's first report,[61] which only reports the first at ca. 1000 cm^{-1}. The difference is attributed to the higher purity of our natural sample, whereas synthetic samples often contain

https://dx.doi.org/10.1021/acs.jpcc.0c04563
J. Phys. Chem. C 2020, 124, 18335−18345

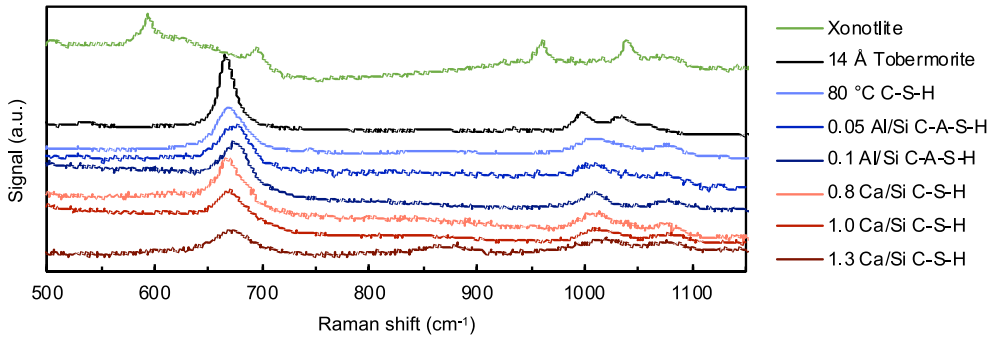

Figure 2. Ambient Raman spectra for xonotlite, 14 Å tobermorite, and calcium−(alumino−)silicate−hydrates (C−(A−)S−H) with varying compositions.

small amounts of $CaCO_3$. This is supported by our simulations (see Movies S1−S4), which show eigenmodes very close to the experimentally observed values (ca. 993, 996, 1031, and 1058 cm^{-1}). The simulation results had no fitting parameters to align the vibrational frequencies determined *in silico* with those observed experimentally. Inspection of these eigenmodes shows that all are associated with Si−O bonds and are not necessarily located on any particular part of the structure. There is a modest dependence of the modes' spectral intensity with the polarization of the incident light (Figure S4), and thus, slight changes in the relative intensity of Si−O stretching at elevated pressure in the crystalline phases (tobermorite, xonotlite) could be assigned to orientation effects as we sample different crystals in the diamond anvil cell gasket.

All C−(A−)S−H samples have a peak at ∼1010 cm^{-1}. This peak is assigned to all Q^2 Si−O stretches (rather than bridging or paired) because the peak intensity does not correlate with the fraction of bridging Q^2 (bridging Q^2 makes up 7% of Si in 0.1 Al/Si C−A−S−H, 10−20% in C−S−H samples). Differences in the anharmonicity of this peak depend on the chemical environment of the silica chains, especially the interlayer, because the sheet of calcium and oxygen ions between the silica chains in the hydrated product is essentially isostructural for all samples.

The 80 °C C−(A−)S−H samples, and the 0.8 and 1.0 Ca/Si C−S−H samples have signals almost entirely from Q^2 tetrahedra, while the 1.3 Ca/Si C−S−H sample also has a signal from Q^1 tetrahedra, in good agreement with previous nuclear magnetic resonance (NMR) characterizations[13] which showed Q^1 populations of 10% in 0.8 Ca/Si, 38% in 1.0 Ca/Si, and 71% in 1.3 Ca/Si. The Q^3 fraction is insignificant in all samples, including the 0.1 Al/Si C−A−S−H. In supporting this work, we characterized the 0.05 Al/Si C−(A−)S−H sample using a standard method,[13] finding quite similar results to the 0.1 C−(A−)S−H sample in terms of cross-linking and Q^1 population (Figure S5, Table S6).

There is modest intensity near 1070 cm^{-1} corresponding to calcium carbonates in the C−(A−)S−H samples;[11] thermogravimetric analysis (TGA) and X-ray diffraction analyses show that these phases make up less than 2% of the powders.[23] Although this peak has previously been shown to grow—maintaining constant width—when the sample was exposed to CO_2, we do not expect carbonation to occur during our analysis, because carbonation takes place over days to weeks, whereas all samples were analyzed over the course of hours to days while in a hermetically sealed diamond anvil cell. This peak was deconvoluted from the analysis of the Q^2 symmetric stretch.

The peak at 3611 cm^{-1} in xonotlite is assigned to the O−H bond stretch in xonotlite. No other samples showed any intensity in this region at ambient pressure or when pressurized up to 6 GPa in silicone oil medium. There is no evidence of $Ca(OH)_2$-like structures which would appear at 3620 cm^{-1} at ambient pressure.[11] Further, we do not observe any portlandite peaks from HP XRD.

High-Pressure Raman Spectra. Figures S6−S13 provide representative raw high-pressure spectra of the xonotlite, 14 Å tobermorite, 80 °C C−S−H, 0.05 Al/Si C−A−S−H, 0.1 Al/Si C−A−S−H, and 0.8, 1.0, and 1.3 Ca/Si C−S−H samples, respectively, in each of the pressure media. The presence of sharp $CaCO_3$ peaks in the 80 °C C−S−H and 0.1 Al/Si C−A−S−H samples is a product of sampling slightly different portions of the sample chamber toward maximizing sample signal, which occasionally led to sampling a volume that contained a small amount of a crystalline $CaCO_3$ phase. In all samples the ambient frequencies were recovered upon decompression. Peak widths are approximately constant over the examined pressure range. The Q^1 tetrahedral peak was not resolvable under pressure because of low signal and overlap from solvent peaks. There are no sharp O−H stretch frequencies observed under ambient or hydrostatic pressure for any samples except xonotlite. The O−H stretch frequency in xonotlite as a function of pressure is given in Figure S14. The high-pressure XRD results of xonotlite used to support this work are given in Figures S15 and S16.

Interlayer Water Packing Density by Thermogravimetric Analysis. Figure 3 shows the basal spacings and interlayer water contents of various crystalline materials, as well as the same qualities of C−(A−)S−H samples obtained from

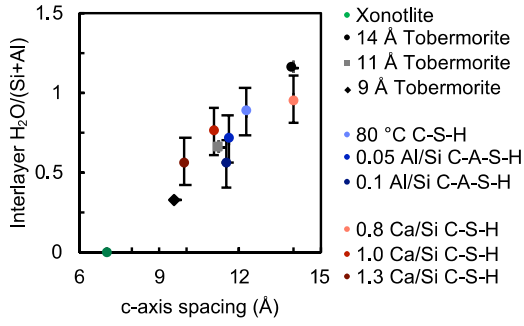

Figure 3. Interlayer water content of the samples in this work as determined experimentally by deconvolution of thermogravimetric analyses.[13,62] For comparison, 14 Å,[18] 11 Å,[63] and 9 Å[64] tobermorite are also included.

https://dx.doi.org/10.1021/acs.jpcc.0c04563
J. Phys. Chem. C 2020, 124, 18335−18345

their diffraction patterns and interlayer water content as determined by deconvolution of TGA data. Separating the TGA spectra of the samples into a Gaussian-shaped weakly bound "gel" water and a tightly bound interlayer water[13,62] shows exceptional agreement with crystalline samples of similar structure, with points essentially on the line between 14 Å tobermorite—representing the greatest degree of hydration in all crystalline tobermorites—and xonotlite, which represents the fully dehyrated example. The reduced number of interlayer water molecules in 0.8 Ca/Si C−S−H compared to 14 Å tobermorite is a result of the increased interlayer Ca^{2+} needed to charge balance the additional Q^1 tetrahedra in the C−S−H. The C−A−S−H samples require fewer water molecules to achieve their basal spacing because of the cross-linked silicate chains occupying the interlayer volume.

Si−O−Si Bending. The pressure dependence of the Q^2 silica tetrahedra bending frequency and the associated properties are given in Table 3. The volume change associated with this bending vibration (eq 2) is in the *bc*-plane. Therefore, the mode Grüneisen parameter is defined using the strain of the *bc*-plane. The compressibility of the plane is calculated using the compressibility in each orthogonal axis and applying the small strain approximation. In xonotlite, the bending is in the *ab*-plane for both Q^2 and Q^3, so the relative strain of the *ab*-plane is used for normalization of both. The strain in a plane is calculated from the compressibility of each crystal axis as determined by separate high-pressure X-ray diffraction experiments.[6,23,44] The high-pressure Raman data points can be found in Figure S17. There is little difference in the anharmonicity of this mode between samples. In comparing the C−S−H samples, the difference in the shift with pressure is compensated by the difference in compressibility of the *c*-axis so that the values are nearly the same.

Table 3. Mode Grüneisen Parameter Pressure Shift for Q^2 Bending Modes in Silica Tetrahedra. Values in Parentheses Are Standard Error of the Fit Slope

sample	ω_0 (cm^{-1})	$d\omega/dP$ (cm^{-1}/GPa)	γ_i (−)
xonotlite, Q^2	695	1.4 (0.07)	0.3
xonotlite, Q^3 (*a*-axis)	593	2.6 (0.08)	0.5
14 Å tobermorite[44]	668	2.8 (0.25)	0.3
80 °C C−S−H[6]	670	3.1 (0.36)	0.4
0.05 Al/Si C−A−S−H[6]	673	2.8 (0.41)	0.5
0.1 Al/Si C−A−S−H[6]	675	2.4 (0.35)	0.5
0.8 Ca/Si C−S−H[23]	668	3.1 (0.33)	0.3
1.0 Ca/Si C−S−H[23]	669	2.8 (0.28)	0.4
1.3 Ca/Si C−S−H[23]	671	2.2 (0.23)	0.4

Si−O symmetric stretch: Experimental and Calculated. The pressure dependence of the Si−O symmetric stretching peaks in each sample is given in Figure S18, and the shifts are summarized in Table 4. The mode Grüneisen parameter was calculated for the volume change of the silica chains. To determine the volume change with pressure, we used the small strain assumption and combined the compressibility in the *a*-axis (measured by HP XRD) and the intralayer portion of the *c*-axis (estimated using CSH-FF),[23] which is approximately 350 GPa^{-1} for each sample. While this normalization is not perfect, it is more meaningful than using the bulk modulus or the compressibility of the *c*-axis because the vibrational amplitude is localized on Si−O stretches.[32] Whatever errors exist in the normalization are systematic so that the normalization affects the results in the same way for each sample, and thus the comparisons between samples are meaningful.

Table 4. Mode Grüneisen Parameter and Related Variables for Symmetric Si−O Stretching[a]

sample	ω_0 (cm^{-1})	$d\omega/dP$ (cm^{-1}/GPa), expt	γ_i (−)	$d\omega/dP$ (cm^{-1}/GPa), CSH-FF
xonotlite	1070	4.3 (0.40)	0.6	
xonotlite	1040	6.4 (0.25)	0.9	11.0
xonotlite	960	6.7 (0.23)	0.9	
14 Å tobermorite	1058	5.2 (0.45)	0.8	12.1
14 Å tobermorite	1033	3.0 (0.33)	0.5	12.1
14 Å tobermorite	998	8.0 (0.50)	1.2	10.3
11 Å tobermorite	1040			13.3
80 °C C−S−H[6]	1012	6.5 (0.42)	1.1	
0.05 Al/Si C−A−S−H[6]	1011	6.0 (0.72)	1.0	
0.1 Al/Si C−A−S−H[6]	1009	5.5 (0.44)	0.9	
0.8 Ca/Si C−S−H	1010	8.1 (0.59)	1.4	12.1
1.0 Ca/Si C−S−H	1015	7.1 (0.80)	1.2	9.4
1.3 Ca/Si C−S−H	1016	6.8 (0.47)	1.1	7.9

[a]ω_0 for 11 Å tobermorite is from CSH-FF. The CSH-FF calculation of the C−S−H samples should be considered qualitative because of the intentional differences between the physical and simulated samples. Values in parentheses are standard errors of the fit.

To understand the differences observed between the samples, we turn to molecular simulations for molecular-level insight. A series of model C−S−H molecules were generated with varying defect concentration and interlayer water content[23] as well as xonotlite and 14 Å tobermorite. These have approximately the same Ca/Si ratio as the C−S−H samples but have an exaggerated water content, so they should not be considered exact replicas of the physical samples. Frequencies in the range of Si−O symmetric stretches were targeted for all samples studied. If there were multiple ambient frequencies predicted by the force field, as in 14 Å tobermorite and xonotlite, the frequencies that were clustered nearest the experimental ambient frequency were chosen to determine $d\omega/dP$. See the Methods section for simulation details and Figures S19−S23 for full vibrational data. Values are given in Table 4.

When comparing the 14 Å tobermorite with C−S−H, we will focus on the Q^2 symmetric stretch ~998 cm^{-1} because this stretch is most easily compared with the C−S−H peak. If C−S−H has the peaks near 1030 and 1060 cm^{-1}, they are not resolvable, partly because of low intensity and partly because of overlap from the unavoidable $CaCO_3$ peak.

Experimental and calculated Grüneisen parameters are given as a function of water content in Figure 4. There is a clear trend toward greater anharmonicity with increasing water content in the interlayer, observed within both series of experiment samples and the CSH-FF samples. The high-pressure vibrational data show that samples with more interlayer water molecules scatter thermal energy more

https://dx.doi.org/10.1021/acs.jpcc.0c04563
J. Phys. Chem. C 2020, 124, 18335−18345

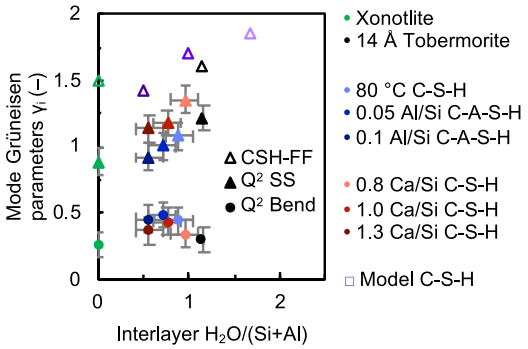

Figure 4. Relationship between the silicate mode Grüneisen parameters and water content. Samples grouped together in the legend represent a series of aluminum content and calcium content. Water content *in silico* is defined by the simulation space while water content in physical samples is determined by crystal structure, in the case of xonotlite and 14 Å tobermorite, and by deconvolution of thermogravimentric data, in the case of C−(A−)S−H samples. Mode Gruneisen error bars are ∼0.1, representing the typical standard error of the fit slope, uncertainty from the calibration, and the standard error of the fit mechanical properties.

efficiently (eqs 4a, 4b). This heuristic is a roadmap toward controlling the thermal properties of concrete by physically separating the sheets with molecules so that even more constituents can fill the interlayer to scatter thermal energy.

In our analysis we do not see a clear correlation between the anharmonicity of the bending mode and the stretching mode. However, given the existing literature of high pressure Raman of a series of glasses[36−39,65] that consistently shows that changes in material composition result in systematic changes in vibrational properties, the results from the symmetric stretch can be assumed to apply to the lower-frequency modes (<600 cm^{-1}) that are responsible for most heat transfer in C−(A−)S−H.[7] Previous work has shown that the mean free path of phonons in C−(A−)S−H is limited by phonon−phonon scattering. Phonon−phonon scattering by the interlayer is the limiting phenomenon for long-wavelength phonons *and* phonons propogating on Si−O bonds (see Table 2, Figure 6 of ref 4.), so interlayer-induced anharmonicity of Si−O stretches is a reasonable proxy for anharmonicity of longer wavelength phonons. More work is needed to study the lowest-wavenumber "basal peak" (which requires special optical filters to measure) because it may provide more insights into heat transport in disordered materials.[66]

Our findings are in good agreement with the mesoscale modeling of Zhang et al.,[67] who measured the effective thermal conductivity in concrete prepared with varying water-to-cement ratios, finding that increasing the water-to-cement ratio (which increases C−S−H basal spacing in more dilute synthesis conditions[68]) decreased the concrete thermal conductivity by 40%, an amount that cannot be explained just using porosity differences using the Maxwell two-phase model, as the porosity effect only accounts for half of the difference.[69] Increasing the number of interlayer constituents is a promising design consideration for improving thermal scattering in cement hydrates.

The simulation has poor agreement for xonotlite compared to 14 Å tobermorite. The divergence is due to the more covalent nature of the bonds in xonotlite. The 14 Å tobermorite vibrations that have more covalent character (ω_0 = 1033, 1058 cm^{-1}) are not reproduced as well as the vibration with more ionic-like character (ω_0 = 998 cm^{-1}); in fact, the deviation is in the opposite direction from the experiment for these covalent-like silicate symmetric stretches.

To examine whether cross-linking, rather than the absence of interlayer water molecules, is the origin of the difference between experimental and calculated anharmonicity in xonotlite, we examine a Merlino 11 Å tobermorite[63] simulation cell because it has cross-linked silicates *and* water molecules. The calculated mechanical properties of the *a*-, *b*-, and *c*- axes are given in Figure S24a. The compressibility of the axes compare well with other structures.[23]

However, the frequency of the 11 Å tobermorite silicate stretch with ω_0 = 1040 cm^{-1} increases much more with pressure than any experimental sample, yielding an unreasonable Grüneisen parameter of 1.9 (Figure S24b). We do not have access to a physical specimen of 11 Å tobermorite, but we can expect that it will have a mode Grüneisen parameter between xonotlite and 14 Å tobermorite (1.2−0.9, respectively), given the structural similarities. An alternate estimate would be to use the properties of 0.05−0.1 Al/Si C−A−S−H, which have cross-linking and a similar basal spacing to 11 Å tobermorite. This estimate also puts its mode Grüneisen parameter close to unity. The unreasonably high anharmonicity calculated by CSH-FF for 11 Å tobermorite shows that the nature of the cross-linked silicate chains is still effectively electrostatic in CSH-FF, and C−(A−)S−H structures that are cross-linked appear to be more thermally insulating *in silico* than their physical counterparts.

Within the C−(A−)S−H samples, the CSH-FF simulation reproduces the trend of increasing anharmonicity with increasing water content (Figure 4). The slope on Figure 4 of the Grüneisen parameter with interlayer H_2O is nearly the same for experimental and CSH-FF points, vindicating the water−CSH interactions,[22] but the extrapolated intercept for the calculated points is higher than for the experimental points, which means that there is intrinsic anharmonicity in the Si, O, Ca, interactions not fully captured by the electrostatic CSH-FF. Stiffening Si−O interactions would improve transferability to the xonotlite, 11 Å tobermorite, and the higher frequency vibrations in 14 Å tobermorite. This calls for a reparametrization of the force field with covalent Si−O bonds explicitly included.

Comparing the bulk modulus of the samples with the anharmonicity of silicate stretching mode reproduces the familiar trend that increasing strength tends to decrease thermal scattering (Figure 5), but also provides an insight for the design of high-strength, low thermal conductivity cements. Moving from the blue C−(A−)S−H samples to the red C−S−H increases strength (as bulk modulus) *and* thermal scattering (as mode Grüneisen parameter). The essential difference between the two is that the C−S−H samples' interlayers are full of water and charge-balancing ions, whereas the C−(A−)S−H samples' interlayers are full of cross-linked chains. This is essentially the same design principle outlined above: bulky interlayers could provide better thermal resistance and comparable strength.

■ CONCLUSIONS

The high-pressure Raman spectroscopy of eight calcium silicate hydrate specimens: xonotlite; 14 Å tobermorite; C−S−H with Ca/Si ratios 0.8, 1.0, and 1.3; and C-A−S-H with Al/Si = 0, 0.05, and 0.1 is investigated toward determining how structural elements bestow bond anharmonicity.

https://dx.doi.org/10.1021/acs.jpcc.0c04563
J. Phys. Chem. C 2020, 124, 18335−18345

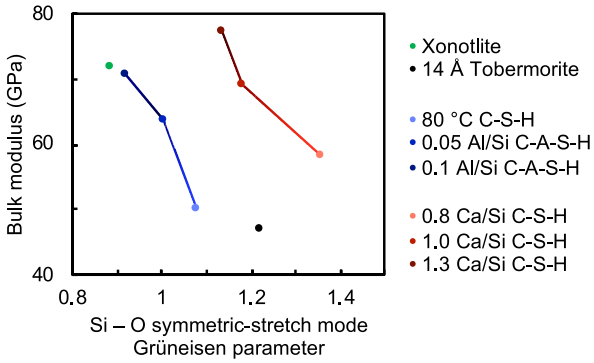

Figure 5. Bulk modulus of samples as determined experimentally, by high-pressure X-ray diffraction, and calculated, by CSH-FF, versus the experimental and calculated silicate symmetric stretching anharmonicity. Series of similar samples are connected by gradient lines.

The anharmonicity of the Q^2 stretching modes is found to increase with increasing interlayer $H_2O/(Si+Al)$, and this phenomenon is also observed in atomistic simulations of these materials. The interlayer constituents physically separating the sheets increase thermal scattering, and we expect that other interlayer constituents will have a similar effect commensurate with their size. Therefore, we suggest C−(A−)S−H architectures that will incorporate a greater volume of interlayer constituents, for example, with siloxanes[70] or compatible polymers,[71−73] that will sterically hinder the opposing layers from approaching. Further characterization, such as thermal conductivity measurements and high-pressure Raman spectroscopy of low-energy vibrations (especially near the Boson peak[4]) is needed to explore this relationship further.

There is a curious problem with cross-linked silicate samples in CSH-FF. Experimentally, we know that cross-linking reduces the anharmonicity through the Al/Si series (blue, Figure 5). This makes physical sense: a cross-linked structure uses opposing bridging Si−O−Si or Si−O−Al, which is a classic covalent interaction, whereas a non-cross-linked structure balances the bridging tetrahedron with a calcium ion, which is an electrostatic interaction. However, in CSH-FF the cross-linked samples of xonotlite and 11 Å tobermorite appear to be the most anharmonic of all, with the silicate stretching mode Grüneisen parameter of nearly two in each calculation, in contrast to experimental values near unity. The case of cross-linked samples highlights the need to optimize the Si − O interaction in a force field. We propose that the Si−O potential could be optimized toward the anharmonicity observed here, especially for the 14 Å tobermorite and/or the xonotlite sample, without affecting the other interatomic potentials. One possible approach is to incorporate functional forms capable of modeling the observed anharmonicity (e.g., the Morse potential[74]) in addition to the existing nonbonded and bonded potentials in the force-field. Some fitting would be required to obtain parameters for the new interactions and fine-tune the existing ones.

High-pressure Raman spectroscopy is demonstrated to be a useful tool for providing chemical bond-level information about the mechanical and thermal properties of nanocrystalline cement minerals. The technique could be used to provide molecular-level understanding of how composite materials in cements (incorporating, e.g., polymers,[71−73] graphene oxide,[75,76] organosilanes,[70] cenospheres[77]) influence the mechanical and thermal properties of cements toward the development of concretes with reduced environmental impact worldwide.

■ ASSOCIATED CONTENT

Supporting Information

The Supporting Information is available free of charge at https://pubs.acs.org/doi/10.1021/acs.jpcc.0c04563.

Mechanical properties of all samples, calibration of the pressure standard, example of fit curve for TGA analysis and fit parameters for TGA analysis, details for atomistic simulations, 29Si NMR characterization results, higher-resolution Raman spectra of 14 Å tobermorite crystal(s), high pressure Raman spectra of all samples, xonotlite OH peak position, CSH-FF xonotlite simulation, HP XRD xonotlite results, Raman peak position vs pressure for all samples, vibrational energy shift with pressure as calculated by CSH-FF, and CSH-FF calculations of 11 Å tobermorite cell parameters and vibrational properties (PDF)

Movie of simulation cell for the lattice vibration at 993 cm^{-1} (MOV)

Movie of simulation cell for the lattice vibration at 996 cm^{-1} (MOV)

Movie of simulation cell for the lattice vibration at 1033 cm^{-1} (MOV)

Movie of simulation cell for the lattice vibration at1058 cm^{-1} (MOV)

■ AUTHOR INFORMATION

Corresponding Author

Carlo Carraro − *University of California Berkeley, Deparment of Chemical and Biomolecular Engineering, Berkeley, California 94720, United States;* orcid.org/0000-0002-3482-9226; Phone: (510) 643-3489; Email: Carraro@berkeley.edu

Authors

David W. Gardner − *University of California Berkeley, Deparment of Chemical and Biomolecular Engineering, Berkeley, California 94720, United States;* orcid.org/0000-0001-9351-8391

Jiaqi Li − *University of California Berkeley, Department of Civil and Environmental Engineering, Berkeley, California 94720, United States;* orcid.org/0000-0003-4863-6641

Ali Morshedifard − *Department of Civil and Environmental Engineering, Henry Samueli School of Engineering, University of California Irvine, Irvine, California 92697, United States*

Saeed Masoumi − *Department of Civil and Environmental Engineering, Henry Samueli School of Engineering, University of California Irvine, Irvine, California 92697, United States*

Mohammad Javad Abdolhosseini Qomi − *Department of Civil and Environmental Engineering, Henry Samueli School of Engineering, University of California Irvine, Irvine, California 92697, United States;* orcid.org/0000-0001-6911-0994

Paulo J. M. Monteiro − *University of California Berkeley, Department of Civil and Environmental Engineering, Berkeley, California 94720, United States;* orcid.org/0000-0002-6866-1783

Roya Maboudian − *University of California Berkeley, Deparment of Chemical and Biomolecular Engineering, Berkeley, California 94720, United States*

Complete contact information is available at: https://pubs.acs.org/10.1021/acs.jpcc.0c04563

https://dx.doi.org/10.1021/acs.jpcc.0c04563
J. Phys. Chem. C 2020, 124, 18335−18345

Notes

The authors declare no competing financial interest.

■ ACKNOWLEDGMENTS

We thank Prof. Garbev for the 14 Å tobermorite sample, and Prof. Barbara Lothenbach for the synthetic C−(A−)S−H samples that were synthesized by Rupert J. Myers and Emilie L'Hôpital at the Laboratory for Concrete & Construction Chemistry. The support of the National Science Foundation under the SusCHEM program, Grant No. 1410557, and under the Division of Materials Research Ceramics Program, DMR-CER, Grant No. 1935604, is gratefully acknowledged. M.J.A.Q. and A.M.'s contribution was supported by the National Science Foundation under Grant No. 1826122. D.W.G. also acknowledges the support by the U.S. Department of Energy, Office of Science, Office of Workforce Development for Teachers and Scientists, Office of Science Graduate Student Research (SCGSR) program. The SCGSR program is administered by the Oak Ridge Institute for Science and Education (ORISE) for the DOE. ORISE is managed by ORAU under Contract No. DE-SC0014664. All opinions expressed in this paper are the authors' and do not necessarily reflect the policies and views of DOE, ORAU, or ORISE. The Advanced Light Source is supported by the Director, Office of Science, Office of Basic Energy Sciences, of the U.S. Department of Energy under Contract No. DE-AC02-05CH11231. Sample preparation of this research was partially supported by COMPRES, the Consortium for Materials Properties Research in Earth Sciences under NSF Cooperative Agreement EAR 1606856. Beamline 12.2.2 is partially supported by COMPRES, the Consortium for Materials Properties Research in Earth Sciences under NSF Cooperative Agreement EAR 1606856. Work at the Molecular Foundry was supported by the Office of Science, Office of Basic Energy Sciences, of the U.S. Department of Energy under Contract No. DE-AC02-05CH11231.

■ REFERENCES

(1) Flatt, R. J.; Roussel, N.; Cheeseman, C. R. Concrete: An Eco Material That Needs to Be Improved. *J. Eur. Ceram. Soc.* **2012**, *32*, 2787−2798.

(2) Miller, S. A.; Horvath, A.; Monteiro, P. J. M. Readily Implementable Techniques Can Cut Annual CO2 Emissions from the Production of Concrete by over 20%. *Environ. Res. Lett.* **2016**, *11*, 074029.

(3) Monteiro, P. J. M.; Miller, S. A.; Horvath, A. Towards Sustainable Concrete. *Nat. Mater.* **2017**, *16*, 698−699.

(4) Abdolhosseini Qomi, M. J.; Ulm, F. J.; Pellenq, R. J. M. Physical Origins of Thermal Properties of Cement Paste. *Phys. Rev. Appl.* **2015**, *3*, 064010.

(5) Richardson, I. G. The Calcium Silicate Hydrates. *Cem. Concr. Res.* **2008**, *38*, 137−158.

(6) Geng, G.; Myers, R. J.; Li, J.; Maboudian, R.; Carraro, C.; Shapiro, D. A.; Monteiro, P. J. M. Aluminum-Induced Dreierketten Chain Cross-Links Increase the Mechanical Properties of Nanocrystalline Calcium Aluminosilicate Hydrate. *Sci. Rep.* **2017**, *7*, 44032.

(7) Zhou, Y.; Morshedifard, A.; Lee, J.; Abdolhosseini Qomi, M. J. The Contribution of Propagons and Diffusons in Heat Transport through Calcium-Silicate-Hydrates. *Appl. Phys. Lett.* **2017**, *110*, 043104.

(8) Khan, M. I. Factors Affecting the Thermal Properties of Concrete and Applicability of Its Prediction Models. *Build. Environ.* **2002**, *37* (6), 607−614.

(9) Wu, Y.; Wang, J. Y.; Monteiro, P. J. M.; Zhang, M. H. Development of Ultra-Lightweight Cement Composites with Low Thermal Conductivity and High Specific Strength for Energy Efficient Buildings. *Constr. Build. Mater.* **2015**, *87*, 100−112.

(10) Abdolhosseini Qomi, M. J.; Krakowiak, K. J.; Bauchy, M.; Stewart, K. L.; Shahsavari, R.; Jagannathan, D.; Brommer, D. B.; Baronnet, A.; Buehler, M. J.; Yip, S.; et al. Combinatorial Molecular Optimization of Cement Hydrates. *Nat. Commun.* **2014**, *5*, 1−10.

(11) Ortaboy, S.; Li, J.; Geng, G.; Myers, R. J.; Monteiro, P. J. M.; Maboudian, R.; Carraro, C. Effects of CO_2 and Temperature on the Structure and Chemistry of C−(A−)S−H Investigated by Raman Spectroscopy. *RSC Adv.* **2017**, *7*, 48925−48933.

(12) Renaudin, G.; Russias, J.; Leroux, F.; Frizon, F.; Cau-dit-Coumes, C. Structural Characterization of C-S-H and C-A-S-H Samples-Part I: Long-Range Order Investigated by Rietveld Analyses. *J. Solid State Chem.* **2009**, *182*, 3312−3319.

(13) L'Hopital, E.; Lothenbach, B.; Kulik, D. A.; Scrivener, K. Influence of Calcium to Silica Ratio on Aluminum Uptake in Calcium Silicate Hydrate. *Cem. Concr. Res.* **2016**, *85*, 111−121.

(14) Youssef, M.; Pellenq, R. J.; Yildiz, B. Glassy Nature of Water in an Ultraconfining Disordered Material: The Case of Calcium−Silicate−Hydrate. *J. Am. Chem. Soc.* **2011**, *133*, 2499−2510.

(15) Bonaccorsi, E.; Merlino, S.; Kampf, A. R. The Crystal Structure of Tobermorite 14 Å (Plombierite), a C-S-H Phase. *J. Am. Ceram. Soc.* **2005**, *88*, 505−512.

(16) Momma, K.; Izumi, F. VESTA 3 for Three-Dimensional Visualization of Crystal, Volumetric and Morphology Data1 K. Momma and F. Izumi. *J. Appl. Crystallogr.* **2011**, *44*, 1272−1276.

(17) Hejny, C.; Armbruster, T. Polytypism in Xonotlite Ca6Si6O17-(OH)2. *Z. Kristallogr. - Cryst. Mater.* **2001**, *216*, 396−408.

(18) Shahsavari, R.; Pellenq, R. J. M.; Ulm, F. J. Empirical Force Fields for Complex Hydrated Calcio-Silicate Layered Materials. *Phys. Chem. Chem. Phys.* **2011**, *13*, 1002−1011.

(19) Cygan, R. T.; Liang, J.-J.; Kalinichev, A. G. Molecular Models of Hydroxide, Oxyhydroxide, and Clay Phases and the Development of a General Force Field. *J. Phys. Chem. B* **2004**, *108*, 1255−1266.

(20) Van Duin, A. C. T.; Dasgupta, S.; Lorant, F.; Goddard, W. A. ReaxFF: A Reactive Force Field for Hydrocarbons. *J. Phys. Chem. A* **2001**, *105*, 9396−9409.

(21) Mishra, R. K.; Mohamed, A. K.; Geissbühler, D.; Manzano, H.; Jamil, T.; Shahsavari, R.; Kalinichev, A. G.; Galmarini, S.; Tao, L.; Heinz, H.; et al. Cemff: A Force Field Database for Cementitious Materials Including Validations, Applications and Opportunities. *Cem. Concr. Res.* **2017**, *102*, 68−89.

(22) Morshedifard, A.; Masoumi, S.; Abdolhosseini Qomi, M. J. Nanoscale Origins of Creep in Calcium Silicate Hydrates. *Nat. Commun.* **2018**, *9*, 1785.

(23) Geng, G.; Myers, R. J.; Qomi, M. J. A.; Monteiro, P. J. M. Densification of the Interlayer Spacing Governs the Nanomechanical Properties of Calcium-Silicate-Hydrate. *Sci. Rep.* **2017**, *7*, 1−8.

(24) Pustovgar, E.; Sangodkar, R. P.; Andreev, A. S.; Palacios, M.; Chmelka, B. F.; Flatt, R. J.; D'Espinose De Lacaillerie, J. B. Understanding Silicate Hydration from Quantitative Analyses of Hydrating Tricalcium Silicates. *Nat. Commun.* **2016**, *7*, 10952.

(25) Kumar, A.; Walder, B. J.; Kunhi Mohamed, A.; Hofstetter, A.; Srinivasan, B.; Rossini, A. J.; Scrivener, K.; Emsley, L.; Bowen, P. The Atomic-Level Structure of Cementitious Calcium Silicate Hydrate. *J. Phys. Chem. C* **2017**, *121*, 17188−17196.

(26) Loudon, R. The Raman Effect in. *Adv. Phys.* **1964**, *13* (52), 423−482.

(27) Ferralis, N.; Maboudian, R.; Carraro, C. Evidence of Structural Strain in Epitaxial Graphene Layers on 6H-SiC(0001). *Phys. Rev. Lett.* **2008**, *101*, 156801.

(28) Fréchette, J.; Carraro, C. Diameter-Dependent Modulation and Polarization Anisotropy in Raman Scattering from Individual Nanowires. *Phys. Rev. B: Condens. Matter Mater. Phys.* **2006**, *74*, 161404.

(29) Garbev, K.; Stemmermann, P.; Black, L.; Breen, C.; Yarwood, J.; Gasharova, B. Structural Features of C-S-H(I) and Its Carbonation in Air-A Raman Spectroscopic Study. Part I: Fresh Phases. *J. Am. Ceram. Soc.* **2007**, *90*, 900−907.

https://dx.doi.org/10.1021/acs.jpcc.0c04563
J. Phys. Chem. C 2020, 124, 18335−18345

(30) Black, L.; Breen, C.; Yarwood, J.; Garbev, K.; Stemmermann, P.; Gasharova, B. Structural Features of C-S-H(I) and Its Carbonation in Air-A Raman Spectroscopic Study. Part II: Carbonated Phases. *J. Am. Ceram. Soc.* **2007**, *90*, 908−917.
(31) Gouadec, G.; Colomban, P. Raman Spectroscopy of Nanomaterials: How Spectra Relate to Disorder, Particle Size and Mechanical Properties. *Prog. Cryst. Growth Charact. Mater.* **2007**, *53*, 1−56.
(32) Hofmeister, A. M.; Mao, H. -k. Redefinition of the Mode Gruneisen Parameter for Polyatomic Substances and Thermodynamic Implications. *Proc. Natl. Acad. Sci. U. S. A.* **2002**, *99*, 559−564.
(33) Zhou, Y.; Morshedifard, A.; Lee, J.; Abdolhosseini Qomi, M. J. The Contribution of Propagons and Diffusons in Heat Transport through Calcium-Silicate-Hydrates. *Appl. Phys. Lett.* **2017**, *110*, 043104.
(34) Holland, M. G. Analysis of Lattice Thermal Conductivity. *Phys. Rev.* **1963**, *132*, 2461−2471.
(35) Klemens, P. G. Thermal Conductivity and Lattice Vibrational Modes. *Solid State Phys.* **1958**, *7*, 1−98.
(36) Sato, Y.; Anderson, O. L. A Comparison of the Acoustic and Thermal Grüneisen Parameters for Three Glasses at Elevated Pressure. *J. Phys. Chem. Solids* **1980**, *41* (4), 401−410.
(37) Bogue, R.; Sladek, R. J. Elasticity and Thermal Expansivity of (AgI)x(AgPO3)1-x Glasses. *Phys. Rev. B: Condens. Matter Mater. Phys.* **1990**, *42* (8), 5280−5288.
(38) Hazen, R. M. High-Pressure Research in Mineral Physics. *Eos, Trans. Am. Geophys. Union* **1988**, *69*, 875.
(39) Ferraro, J. R.; Manghnani, M. H. Infrared Absorption Spectra of Sodium Silicate Glasses at High Pressures. *J. Appl. Phys.* **1972**, *43*, 4595−4599.
(40) Regourd, M. Microstructure of High Strength Cement Paste Systems. *Mater. Res. Soc. Symp. Proc.* **1984**, *42*, 3.
(41) Shaw, S.; Clark, S. M.; Henderson, C. M. B. Hydrothermal Formation of the Calcium Silicate Hydrates, Tobermorite and Xonotlite : An in Situ Synchrotron Study. *Chem. Geol.* **2000**, *167*, 129−140.
(42) L'Hôpital, E.; Lothenbach, B.; Scrivener, K.; Kulik, D. A. Alkali Uptake in Calcium Alumina Silicate Hydrate (C-A-S-H). *Cem. Concr. Res.* **2016**, *85*, 122−136.
(43) Li, J.; Geng, G.; Myers, R.; Yu, Y. S.; Shapiro, D.; Carraro, C.; Maboudian, R.; Monteiro, P. J. M. The Chemistry and Structure of Calcium (Alumino) Silicate Hydrate: A Study by XANES, Ptychographic Imaging, and Wide- and Small-Angle Scattering. *Cem. Concr. Res.* **2019**, *115*, 367−278.
(44) Oh, J. E.; Clark, S. M.; Wenk, H. R.; Monteiro, P. J. M. Experimental Determination of Bulk Modulus of 14 Å Tobermorite Using High Pressure Synchrotron X-Ray Diffraction. *Cem. Concr. Res.* **2012**, *42*, 397−403.
(45) Bell, N. S.; Venigalla, S.; Gill, P. M.; Adair, J. H. Morphological Forms of Tobermorite in Hydrothermally Treated Calcium Silicate Hydrate Gels. *J. Am. Ceram. Soc.* **1996**, *79*, 2175−2178.
(46) Baer, B. J.; Chang, M. E.; Evans, W. J. Raman Shift of Stressed Diamond Anvils: Pressure Calibration and Culet Geometry Dependence. *J. Appl. Phys.* **2008**, *104*, 034504.
(47) Myers, R. J.; L'Hôpital, E.; Provis, J. L.; Lothenbach, B. Effect of Temperature and Aluminium on Calcium (Alumino)Silicate Hydrate Chemistry under Equilibrium Conditions. *Cem. Concr. Res.* **2015**, *68*, 83−93.
(48) Masoumi, S.; Valipour, H.; Abdolhosseini Qomi, M. J. Intermolecular Forces between Nanolayers of Crystalline Calcium-Silicate-Hydrates in Aqueous Medium. *J. Phys. Chem. C* **2017**, *121* (10), 5565−5572.
(49) Shalchy, F.; Rahbar, N. Nanostructural Characteristics and Interfacial Properties of Polymer Fibers in Cement Matrix. *ACS Appl. Mater. Interfaces* **2015**, *7*, 17278−17286.
(50) Hou, D.; Ma, H.; Zhu, Y.; Li, Z. Calcium Silicate Hydrate from Dry to Saturated State: Structure, Dynamics and Mechanical Properties. *Acta Mater.* **2014**, *67*, 81−94.
(51) Bonnaud, P. A.; Ji, Q.; Coasne, B.; Pellenq, R. J. M.; Van Vliet, K. J. Thermodynamics of Water Confined in Porous Calcium-Silicate-Hydrates. *Langmuir* **2012**, *28*, 11422−11432.
(52) Geng, G.; Vasin, R. N.; Li, J.; Qomi, M. J. A.; Yan, J.; Wenk, H. R.; Monteiro, P. J. M. Preferred Orientation of Calcium Aluminosilicate Hydrate Induced by Confined Compression. *Cem. Concr. Res.* **2018**, *113*, 186−196.
(53) Bauchy, M.; Wang, B.; Wang, M.; Yu, Y.; Abdolhosseini Qomi, M. J.; Smedskjaer, M. M.; Bichara, C.; Ulm, F. J.; Pellenq, R. Fracture Toughness Anomalies: Viewpoint of Topological Constraint Theory. *Acta Mater.* **2016**, *121*, 234−239.
(54) Masoumi, S.; Valipour, H.; Abdolhosseini Qomi, M. J. Interparticle Interactions in Colloidal Systems: Toward a Comprehensive Mesoscale Model. *ACS Appl. Mater. Interfaces* **2017**, *9* (32), 27338−27349.
(55) Masoumi, S.; Zare, S.; Valipour, H.; Abdolhosseini Qomi, M. J. Effective Interactions Between Calcium-Silicate-Hydrate Nanolayers. *J. Phys. Chem. C* **2019**, *123* (8), 4755−4766.
(56) Masoumi, S.; Valipour, H.; Abdolhosseini Qomi, M. J. Intermolecular Forces between Nanolayers of Crystalline Calcium-Silicate-Hydrates in Aqueous Medium. *J. Phys. Chem. C* **2017**, *121* (10), 5565−5572.
(57) Plimpton, S. Fast Parallel Algorithms for Short-Range Molecular Dynamics. *J. Comput. Phys.* **1995**, *117* (1), 1−19.
(58) Gale, J. D. GULP: A Computer Program for the Symmetry-Adapted Simulation of Solids. *J. Chem. Soc., Faraday Trans.* **1997**, *93* (4), 629−637.
(59) Gale, J. D.; Rohl, A. L. The General Utility Lattice Program (GULP). *Mol. Simul.* **2003**, *29*, 291−241.
(60) Frost, R. L.; Mahendran, M.; Poologanathan, K.; Xi, Y. Raman Spectroscopic Study of the Mineral Xonotlite Ca 6Si 6O 17(OH) 2 - A Component of Plaster Boards. *Mater. Res. Bull.* **2012**, *47*, 3644−3649.
(61) Kirkpatrick, R. J.; Yarger, J.L.; McMillan, P. F.; Ping, Y.; Cong, X. Raman Spectroscopy of C-S-H, Tobermorite, and Jennite. *Adv. Cem. Based Mater.* **1997**, *5* (3−4), 93−99.
(62) Myers, R. J.; L'Hôpital, E.; Provis, J. L.; Lothenbach, B. Composition-Solubility-Structure Relationships in Calcium (Alkali) Aluminosilicate Hydrate (C-(N,K-)A-S-H). *Dalt. Trans.* **2015**, *44*, 13530−13544.
(63) Merlino, S.; Bonaccorsi, E.; Armbruster, T. The Real Structure of Tobermorite 11Å: Normal and Anomalous Forms, OD Character and Polytypic Modifications. *Eur. J. Mineral.* **2001**, *13*, 577−590.
(64) Merlino, S.; Bonaccorsi, E.; Armbruster, T. Tobermorites: Their Real Structure and Order-Disorder (OD) Character. *Am. Mineral.* **1999**, *84* (10), 1613−1621.
(65) Xu, J.; Butler, I. S.; Gilson, D. F. R. FT-Raman and High-Pressure Infrared Spectroscopic Studies of Dicalcium Phosphate Dihydrate (CaHPO4·2H2O) and Anhydrous Dicalcium Phosphate (CaHPO4). *Spectrochim. Acta, Part A* **1999**, *55*, 2801−2809.
(66) Schroeder, J.; Wu, W.; Apkarian, J. L.; Lee, M.; Hwa, L. G.; Moynihan, C. T. Raman Scattering and Boson Peaks in Glasses: Temperature and Pressure Effects. *J. Non-Cryst. Solids* **2004**, *349*, 88−97.
(67) Zhang, W.; Min, H.; Gu, X.; Xi, Y.; Xing, Y. Mesoscale Model for Thermal Conductivity of Concrete. *Constr. Build. Mater.* **2015**, *98*, 8−16.
(68) Chiang, W. S.; Fratini, E.; Baglioni, P.; Liu, D.; Chen, S. H. Microstructure Determination of Calcium-Silicate-Hydrate Globules by Small-Angle Neutron Scattering. *J. Phys. Chem. C* **2012**, *116*, 5055−5061.
(69) Kearsley, E. P.; Wainwright, P. J. The Effect of Porosity on the Strength of Foamed Concrete. *Cem. Concr. Res.* **2002**, *32*, 233−239.
(70) Orozco, C. A.; Chun, B. W.; Geng, G.; Emwas, A. H.; Monteiro, P. J. M. Characterization of the Bonds Developed between Calcium Silicate Hydrate and Polycarboxylate-Based Superplasticizers with Silyl Functionalities. *Langmuir* **2017**, *33*, 3404−3412.
(71) Zhou, Y.; Hou, D.; Manzano, H.; Orozco, C. A.; Geng, G.; Monteiro, P. J. M.; Liu, J. Interfacial Connection Mechanisms in

https://dx.doi.org/10.1021/acs.jpcc.0c04563
J. Phys. Chem. C 2020, 124, 18335−18345

Calcium-Silicate-Hydrates/Polymer Nanocomposites: A Molecular Dynamics Study. *ACS Appl. Mater. Interfaces* **2017**, *9*, 41014−40125.
(72) Raki, L.; Beaudoin, J.; Alizadeh, R.; Makar, J.; Sato, T. Cement and Concrete Nanoscience and Nanotechnology. *Materials* **2010**, *3*, 918−942.
(73) Marchon, D.; Juilland, P.; Gallucci, E.; Frunz, L.; Flatt, R. J. Molecular and Submolecular Scale Effects of Comb-Copolymers on Tri-Calcium Silicate Reactivity: Toward Molecular Design. *J. Am. Ceram. Soc.* **2017**, *100*, 817−841.
(74) Morse, P. M. Diatomic Molecules According to the Wave Mechanics. II. Vibrational Levels. *Phys. Rev.* **1929**, *34*, 57.
(75) Hou, D.; Lu, Z.; Li, X.; Ma, H.; Li, Z. Reactive Molecular Dynamics and Experimental Study of Graphene-Cement Composites: Structure, Dynamics and Reinforcement Mechanisms. *Carbon* **2017**, *115*, 188−208.
(76) Zhu, X. H.; Kang, X. J.; Yang, K.; Yang, C. H. Effect of Graphene Oxide on the Mechanical Properties and the Formation of Layered Double Hydroxides (LDHs) in Alkali-Activated Slag Cement. *Constr. Build. Mater.* **2017**, *132*, 290−295.
(77) Rheinheimer, V.; Wu, Y.; Wu, T.; Celik, K.; Wang, J.; De Lorenzis, L.; Wriggers, P.; Zhang, M. H.; Monteiro, P. J. M. Multi-Scale Study of High-Strength Low-Thermal-Conductivity Cement Composites Containing Cenospheres. *Cem. Concr. Compos.* **2017**, *80*, 91−103.

https://dx.doi.org/10.1021/acs.jpcc.0c04563
J. Phys. Chem. C 2020, 124, 18335−18345